$K\alpha$ absorption spectroscopy: Diagnostic of the radiative preheating of a laser-irradiated layered target

C. Chenais-Popovics, C. Fievet, J. P. Geindre, and J. C. Gauthier
Laboratoire de Physique des Milieux Ionisés and Laboratoire d'Utilisation des Lasers Intenses, Ecole Polytechnique, Palaiseau, France

E. Luc-Koenig and J. F. Wyart
Laboratoire Aimé-Cotton, Université Paris XI, Orsay, France

H. Pépin and M. Chaker
Institut National de la Recherche Scientifique-Energie, Varennes, Québec, Canada
(Received 3 April 1989)

$K\alpha$ absorption spectroscopy has been used to diagnose the low-temperature, high-density region of layered targets (high-Z on low-Z elements) irradiated by 0.26-μm laser light at irradiances between 2×10^{14} and 4×10^{15} W/cm^2. Time-resolved and time-integrated spectra have been recorded from the front and the rear of the target with high spectral resolution in the 1–3-keV range and low spectral resolution in the 40-eV–4-keV range. Experimental results provide measurements of the electron-temperature gradient shape in the region 50–200 eV. A detailed analysis of the atomic structure of He-like to F-like ions of chlorine and aluminum has been performed to give simulated absorption spectra as a function of plasma parameters. We show here a measurement of the shallow electron-temperature gradient around 100 eV built up by the absorption of x rays emitted by the laser-irradiated high-Z layer. This is in very good agreement with results obtained from a one-dimensional hydrocode including photon transport physics.

I. INTRODUCTION

In laser-target interaction, high-resolution x-ray spectroscopy is known as a good diagnostic tool for plasma parameters such as the ionization state and the electronic density and temperature. Emission spectroscopy is widely used but it is mostly limited to the diagnostics of the conduction region and of the corona where the density is low enough for the photons to escape.[1–5] Absorption x-ray spectroscopy has been shown to be an interesting alternative to extend spectroscopic diagnostics to higher density plasmas.[6–10] $K\alpha$ lines are good candidates for such measurements because their wavelengths are characteristic of the ionic distribution of the absorbing plasma. This technique requires the use of an external x-ray source emitting a broadband continuum over the spectral range of absorption lines. Thus, emitter and absorber elements have to be chosen carefully in order to match their respective emission and absorption spectral range.

In this paper we present a detailed analysis of $K\alpha$ absorption spectra of chlorine and aluminum. Experimental data have been obtained by focusing a laser beam onto a target consisting of a high-Z element layer deposited on a foil containing the absorber. The high-Z element emits a complex spectrum covering the xuv (50–1000 eV) and the soft x-ray (1–5 keV) photon energy range. In the xuv range, the emission is very strong and high conversion efficiencies have been measured.[11,12] In the soft x-ray range where chlorine and aluminum $K\alpha$ absorption lines occur, the spectrum of high-Z elements is made up of unresolved transition arrays (UTA) superimposed on top of broad continuum features.[13–17] In this experiment, we have taken advantage of these two emission: the xuv photons are used to heat the dense part of the target and the soft x-ray photons in the 1–3 keV range are used as a backlighter for the absorption spectroscopy diagnostic.

The experimental setup is described in Sec. II. In Sec. III we present atomic structure and population calculations which give the absorption coefficients of the $K\alpha$ lines as a function of plasma parameters. We show also how absorption spectroscopy can give a measurement of the electronic temperature in the absorbing region. In addition, we present a brief description of the hydrodynamic code XRAD used in the simulations. Section IV is devoted to experimental results, measurements of the temperature gradient in the target, and interpretation of the physics of a radiatively heated foil by comparing experimental data to hydrocode results.

II. EXPERIMENTAL SETUP

One beam of the Laboratoire d'Utilisation des Lasers Intenses Laser Facility Nd-glass laser was focused onto a plane layered target. The laser was frequency quadrupled giving 0.26-μm wavelength and 500-ps pulse duration. The laser energy was varied from 10 to 30 J. The focal spot size was changed from shot to shot with a minimum diameter of 80 μm, producing laser intensities in the range 2×10^{14} to 4×10^{15} W/cm^2.

The beam was focused onto a layered target consisting

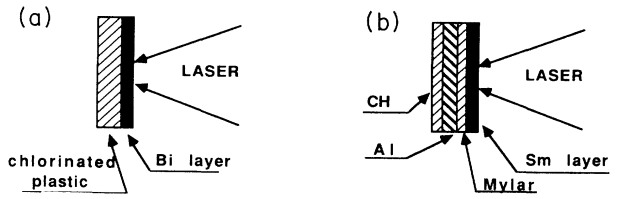

FIG. 1. Targets used in the experiments. (a): Bi-Cl targets; (b): Sm-Al targets; Mylar thickness is varied from 0 to 6 μm.

of a 0.08 to 2-μm bismuth layer deposited on a 12.5-μm-thick chlorinated plastic $(C_2H_2Cl_2)_n$ foil [see Fig. 1(a)]. A complementary experiment has been performed with a thinner absorber layer in order to have a more local measurement of the absorption. A 0.7-μm-thick aluminum layer was buried between Mylar $(C_{10}H_8O_4)$ and parylene $(CH)_n$ layers at different depths (up to 6 μm from the target surface) as shown in Fig. 1(b). In this case, the high-Z backlighter was a 0.4-μm-thick samarium layer which M-band emission lies in the 1.3–1.6 keV spectral range.

Figure 2 shows the different instruments used to record x-ray emission at the front and at the rear of the target. The main diagnostic was crystal spectroscopy using a pentaerythritol (PET) crystal in the 3–5-Å range and an ammonium dihydrogen phosphate ADP crystal in the 6–8-Å range for the chlorine and aluminum experiments, respectively. Two time-integrating crystal spectrometers were used with 200 μm entrance slits, as shown in Fig. 2. Spectra were recorded on Kodak SB-392 films and digitized on a microdensitometer. Conversion of film density to intensity and removal of distortions introduced by the spectrometer geometry were post-processed on a minicomputer using standard procedures.[18,19] A time-resolving spectrograph consisting of a silicon crystal placed in front of the slit of a Kentech x-ray streak camera was used to get the time evolution of the backlighter light and of the absorption features with sweep speeds of 100 ps/mm. The target was tilted in order to be perpendicular to the line of sight of the rear spectrograph (either time integrated or time resolved).

A 2000- and a 1000-lines/mm transmission grating spectrograph[20,21] were also placed at the front and at the rear of the target, respectively. They measured the

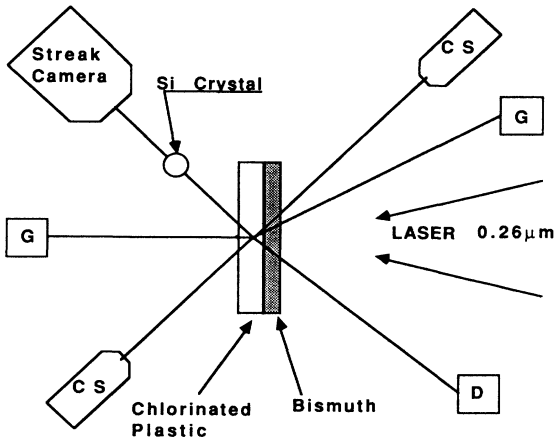

FIG. 2. Set up of the experiment. CS; crystal spectrographs with PET or ADP crystal; G; transmission grating spectrograph; D; filtered diodes array.

broadband spectrum of the x-rays absorbed in the target. Grating resolutions were 10 Å/mm and 20 Å/mm, respectively. Spectra were recorded on 101-01 Kodak films in the range 40–2 keV.

A set of filtered diodes was placed in front of the target to give an absolute value of the emitted x-ray energy. Table I shows the filters used in front of the diodes and the x-ray range covered by this diagnostic. Finally, a pinhole filtered with aluminized Mylar was viewing the target at 45° from the laser axis to measure the size of the laser focal spot.

III. ABSORPTION MODELING

Quantitative measurements can be obtained from absorption spectroscopy by comparing the experimental data to calculated absorption spectra. Three steps can be distinguished in the modeling of these spectra. First, we have calculated the wavelengths and the oscillator strengths of the $K\alpha$ lines. Then, we used a collisional-radiative model to evaluate the ionic populations at a given matter density and electronic temperature. Finally, the plasma optical depth (product of the absorption coefficient by the photon path length) was obtained as a function of photon energy by summing the contribution

TABLE I. Type of diodes, filters, and energy bandwidth of the nine channels used in the diode spectrometer.

	Filter thickness	Diode	Sensitivity region
Al	0.8 μm	X.R.D	0–200 eV+0.5–1.6 keV
CH	1 μm	X.R.D	50–300 eV+0.5–1.7 keV
Ti	2 μm	X.R.D	0.3–0.5 keV+ > 1.2 keV
Fe	1 μm	X.R.D	550–750 eV+ > 1.6 keV
Cu	1 μm	X.R.D	0.55–1.0 keV+ > 1.8 keV
Al	8 μm	X.R.D	0.6–1.5 keV+2.3–3.2 keV
Be	60 μm	X.R.D	1.3–2.6 keV
Ti	20 μm	*p-i-n*	2.7–4.7 keV
Fe	25 μm	*p-i-n*	> 3.7 keV

of each individual $K\alpha$ line.

In this section theoretical spectra will be obtained from a one-temperature, one-density model. The complete analysis of the data will be done in Sec. IV by using this model and taking into account the shape of the electron-temperature gradient.

A. Wavelengths and oscillator strengths

Wavelengths and transition probabilities of the $1s$-$2p$ lines have been calculated with the relativistic parametric potential method,[22,23] which is used in the program RELAC.[24] In this method, the potential due to the radial

TABLE II. Lower and upper states involved in $K\alpha$ lines and their respective J quantum numbers, wavelengths, and gf for chlorine and aluminum. States are labeled in LS coupling and term mixing is indicated (notation $^1D^\circ$ means $S=1$, $L=2$, odd parity).

Lower state		J_l	Upper state		J_u	λ_{Cl}	gf_{Cl}	λ_{Al}	gf_{Al}
			He-like			Cl XVI		Al XII	
$1s^2$	^1S	0	$1s2p$	$^1P^\circ$	1	4.443 17	0.773	7.755 07	0.770
			Li-like			Cl XV		Al XI	
$1s^22s$	^2S	$\frac{1}{2}$	$1s2s2p$	$^2P^\circ$	$\frac{3}{2}$	4.480 31	0.915	7.845 51	0.953
$1s^22p$	$2P^\circ$	$\frac{1}{2}$	$1s2p^2$	^2P	$\frac{1}{2}$	4.485 10	0.513	7.857 92	0.533
$1s^22p$	$^2P^\circ$	$\frac{3}{2}$	$1s2p^2$	^2P	$\frac{3}{2}$	4.485 18	1.29	7.858 02	1.36
$1s^22p$	$^2P^\circ$	$\frac{1}{2}$	$1s2p^2$	^2D	$\frac{3}{2}$	4.489 92	0.529	7.871 81	0.485
$1s^22p$	$^2P^\circ$	$\frac{3}{2}$	$1s2p^2$	^2D	$\frac{5}{2}$	4.493 12	0.700	7.874 82	0.743
			Be-like			Cl XIV		Al X	
$1s^22p^2$	^1D	2	$1s2p^3$	$^1P^\circ$	1	4.513 70	0.620	7.913 40	0.609
$1s^22s^2$	^1S	0	$1s2s^22p$	$^1P^\circ$	1	4.516 07	0.739	7.920 50	0.727
$1s^22s2p$	$^1P^\circ$	1	$1s2s2p^2$	^1P	1	4.521 54	1.13	7.932 38	1.12
$1s^22s2p$	$^3P^\circ$	2	$1s2s2p^2$	^3P	2	4.526 78	1.53	7.945 39	1.50
$1s^22s2p$	$^3P^\circ$	1	$1s2s2p^2$	^3D	2	4.528 12	0.780	7.946 87	0.754
$1s^22s2p$	$^3P^\circ$	2	$1s2s2p^2$	^3D	3	4.529 99	0.857	7.948 45	0.829
$1s^22p^2$	^3P	1	$1s2p^3$	$^3P^\circ$	1	4.531 02	0.585	7.955 23	0.530
$1s^22p^2$	^1D	2	$1s2p^3$	$^1D^\circ+{}^3P^\circ$	2	4.533 03	0.871	7.959 01	0.336
$1s^22p^2$	^3P	2	$1s2p^3$	$^3S^\circ$	1	4.533 26	0.737	7.957 26	0.803
$1s^22p^2$	^1D	2	$1s2p^3$	$^1D^\circ+{}^3P^\circ$	2	4.537 26	1.00	7.964 26	1.51
$1s^22p^2$	^3P	1	$1s2p^3$	$^3D^\circ$	2	4.541 16	0.512	7.976 19	0.464
$1s^22s2p$	$^1P^\circ$	1	$1s2s2p^2$	^1D	2	4.541 75	0.527	7.977 53	0.595
$1s^22p^2$	^3P	2	$1s2p^3$	$^3D^\circ$	3	4.543 11	0.841	7.978 10	0.823
$1s^22p^2$	^1S	0	$1s2p^3$	$^1P^\circ$	1	4.544 17	0.507	7.983 70	0.496
			Be-like			Cl XIII		Al IX	
$1s^22s^22p$	$^2P^\circ$	$\frac{3}{2}$	$1s2s^22p^2$	^2P	$\frac{3}{2}$	4.556 47	1.30	8.010 70	1.24
$1s^22s^22p$	$^2P^\circ$	$\frac{1}{2}$	$1s2s^22p^2$	^2P	$\frac{1}{2}$	4.556 85	0.565	8.010 90	0.522
$1s^22s2p^2$	^2D	$\frac{5}{2}$	$1s2s2p^3$	$^2P^\circ$	$\frac{3}{2}$	4.557 34	0.184	8.011 38	0.617
$1s^22s2p^2$	^4P	$\frac{5}{2}$	$1s2s2p^3$	$^4P^\circ$	$\frac{5}{2}$	4.559 21	0.607	8.013 00	0.536
$1s^22s^22p$	$^2P^\circ$	$\frac{1}{2}$	$1s2s^22p^2$	^2D	$\frac{3}{2}$	4.561 59	0.520	8.022 94	0.443
$1s^22s2p^2$	^2P	$\frac{3}{2}$	$1s2s2p^3$	$^2S^\circ$	$\frac{1}{2}$	4.562 35	0.725	8.023 79	0.710
$1s^22p^3$	$^2D^\circ$	$\frac{3}{2}$	$1s2p^4$	^2P	$\frac{1}{2}$	4.564 21	0.546	8.029 55	0.576
$1s^22s^22p$	$^2P^\circ$	$\frac{3}{2}$	$1s2s^22p^2$	^2D	$\frac{5}{2}$	4.564 45	0.705	8.025 53	0.679
$1s^22p^3$	$^2D^\circ$	$\frac{5}{2}$	$1s2p^4$	^2P	$\frac{3}{2}$	4.566 48	1.18	8.031 85	1.14
$1s^22s2p^2$	^4P	$\frac{3}{2}$	$1s2s2p^3$	$^4P^\circ$	$\frac{3}{2}$	4.568 09	0.752	8.038 15	0.670
$1s^22s2p^2$	^4P	$\frac{5}{2}$	$1s2s2p^3$	$^4S^\circ$	$\frac{3}{2}$	4.570 00	0.848	8.039 77	0.915
$1s^22s2p^2$	^2D	$\frac{5}{2}$	$1s2s2p^3$	$^2D^\circ$	$\frac{5}{2}$	4.571 12	1.86	8.043 50	1.81
$1s^22s2p^2$	^2D	$\frac{3}{2}$	$1s2s2p^3$	$^2D^\circ$	$\frac{3}{2}$	4.571 30	1.13	8.043 55	1.14
$1s^22s2p^2$	^4P	$\frac{3}{2}$	$1s2s2p^3$	$^4D^\circ$	$\frac{5}{2}$	4.572 24	0.587	8.043 84	0.512
$1s^22p^3$	$^2D^\circ$	$\frac{5}{2}$	$1s2p^4$	^2D	$\frac{5}{2}$	4.572 30	0.995	8.043 83	0.961

TABLE II. (*Continued*).

Lower state		J_l	Upper state		J_u	λ_{Cl}	gf_{Cl}	λ_{Al}	gf_{Al}
$1s^2 2p^3$	$^2D^\circ$	$\frac{3}{2}$	$1s2p^4$	^2D	$\frac{3}{2}$	4.572 70	0.830	8.044 13	0.701
$1s^2 2s2p^2$	^4P	$\frac{5}{2}$	$1s2s2p^3$	$^4D^\circ$	$\frac{7}{2}$	4.573 82	0.943	8.045 32	0.901
$1s^2 2p^3$	$^4S^\circ$	$\frac{3}{2}$	$1s2p^4$	^4P	$\frac{5}{2}$	4.576 98	0.701	8.051 30	0.671
$1s^2 2s2p^2$	^2S	$\frac{1}{2}$	$1s2s2p^3$	$^2P^\circ$	$\frac{3}{2}$	4.578 29	0.575	8.059 47	0.567
$1s^2 2s2p^2$	^4P	$\frac{3}{2}$	$1s2s2p^3$	$^4D^\circ$	$\frac{5}{2}$	4.581 14	0.659	8.063 61	0.626
$1s^2 2p^3$	$^2P^\circ$	$\frac{3}{2}$	$1s2p^4$	^2P	$\frac{3}{2}$	4.586 61	0.466	8.077 08	0.535
			C-like			Cl XII		Al VIII	
$1s^2 2s^2 2p^2$	^1D	2	$1s2s^2 2p^3$	$^1P^\circ$	1	4.590 37	0.629	8.084 10	0.610
$1s^2 2s^2 2p^2$	^3P	2	$1s2s^2 2p^3$	$^3S^\circ$	1	4.595 86	0.848	8.095 80	0.799
$1s^2 2s^2 2p^2$	^3P	1	$1s2s^2 2p^3$	$^3P^\circ$	1	4.596 88	0.569	8.096 95	0.508
$1s^2 2s^2 2p^2$	^3P	2	$1s2s^2 2p^3$	$^3P^\circ$	2	4.597 36	0.573	8.097 19	0.490
$1s^2 2s2p^3$	$^1D^\circ$	2	$1s2s2p^4$	^1P	1	4.598 10	0.907	8.099 69	0.878
$1s^2 2s^2 2p^2$	^1D	2	$1s2s^2 2p^3$	$^1D^\circ$	2	4.599 18	1.73	8.102 54	1.68
$1s^2 2s2p^3$	$^3D^\circ$	2	$1s2s2p^4$	^3P	1	4.602 63	0.700	8.111 81	0.381
$1s^2 2s2p^3$	$^3D^\circ$	3	$1s2s2p^4$	^3P	2	4.603 75	0.858	8.116 03	0.936
$1s^2 2s2p^3$	$^3D^\circ$	3	$1s2s2p^4$	^3D	3	4.604 40	1.09	8.112 03	1.04
$1s^2 2s2p^3$	$^3D^\circ$	1	$1s2s2p^4$	^3D	1	4.604 89	0.664	8.114 14	0.451
$1s^2 2s^2 2p^2$	^3P	1	$1s2s^2 2p^3$	$^3D^\circ$	2	4.605 11	0.532	8.114 34	0.455
$1s^2 2s2p^3$	$^3P^\circ$	2	$1s2s2p^4$	^3P	2	4.605 93	0.867	8.147 75	0.623
$1s^2 2s2p^3$	$^3D^\circ$	3	$1s2s2p^4$	^3D	2	4.606 15	0.504	8.111 84	0.387
$1s^2 2s^2 2p^2$	^3P	2	$1s2s^2 2p^3$	$^3D^\circ$	3	4.606 51	0.787	8.115 81	0.751
$1s^2 2s2p^3$	$^5S^\circ$	2	$1s2s2p^4$	^5P	2	4.606 90	0.575	8.117 57	0.544
$1s^2 2p^4$	^1D	2	$1s2p^5$	$^1P^\circ$	1	4.608 75	1.18	8.122 76	1.14
$1s^2 2s2p^3$	$^5S^\circ$	2	$1s2s2p^4$	^5P	3	4.609 00	0.808	8.119 45	0.764
$1s^2 2s2p^3$	$^1P^\circ$	1	$1s2s2p^4$	^1P	1	4.612 41	0.523	8.131 23	0.501
$1s^2 2p^4$	^3P	2	$1s2p^5$	$^3P^\circ$	2	4.614 76	0.854	8.134 25	0.816
$1s^2 2s2p^3$	$^3S^\circ$	1	$1s2s2p^4$	$^3P+{}^1D$	2	4.618 47	0.142	8.136 81	0.522
$1s^2 2s2p^3$	$^1D^\circ$	2	$1s2s2p^4$	^1D	2	4.618 59	0.747	8.145 48	0.860
			N-like			Cl XI		Al VII	
$1s^2 2s^2 2p^3$	$^2D^\circ$	$\frac{3}{2}$	$1s2s^2 2p^4$	^2P	$\frac{1}{2}$	4.630 78	0.466	8.170 67	0.521
$1s^2 2s^2 2p^3$	$^2D^\circ$	$\frac{5}{2}$	$1s2s^2 2p^4$	^2P	$\frac{3}{2}$	4.632 74	1.14	8.172 76	1.07
$1s^2 2s^2 2p^3$	$^2D^\circ$	$\frac{5}{2}$	$1s2s^2 2p^4$	^2D	$\frac{5}{2}$	4.638 06	0.958	8.183 17	0.907
$1s^2 2s^2 2p^3$	$^2D^\circ$	$\frac{3}{2}$	$1s2s^2 2p^4$	^2D	$\frac{3}{2}$	4.638 25	0.849	8.183 40	0.683
$1s^2 2s^2 2p^3$	$^4S^\circ$	$\frac{3}{2}$	$1s2s^2 2p^4$	^4P	$\frac{5}{2}$	4.642 45	0.676	8.189 91	0.634
$1s^2 2s2p^4$	^2D	$\frac{3}{2}$	$1s2s2p^5$	$^2P^\circ$	$\frac{1}{2}$	4.643 35	0.734	8.197 31	0.680
$1s^2 2s2p^4$	^4P	$\frac{5}{2}$	$1s2s2p^5$	$^4P^\circ$	$\frac{5}{2}$	4.644 70	0.945	8.195 35	0.885
$1s^2 2s2p^4$	^2D	$\frac{5}{2}$	$1s2s2p^5$	$^2P^\circ$	$\frac{3}{2}$	4.644 97	1.24	8.198 79	1.19
$1s^2 2s2p^4$	^2P	$\frac{3}{2}$	$1s2s2p^5$	$^2P^\circ$	$\frac{3}{2}$	4.652 38	0.675	8.215 07	0.639
			O-like			Cl X		Al VI	
$1s^2 2s^2 2p^4$	^1D	2	$1s2s^2 2p^5$	$^1P^\circ$	1	4.671 04	1.13	8.249 53	1.07
$1s^2 2s^2 2p^4$	^3P	2	$1s2s^2 2p^5$	$^3P^\circ$	2	4.676 59	0.817	8.259 66	0.762
$1s^2 2s2p^5$	$^3P^\circ$	2	$1s2s2p^6$	^3S	1	4.678 64	0.548	8.264 04	0.507
			F-like			Cl IX		Al V	
$1s^2 2s^2 2p^5$	$^2P^\circ$	$\frac{3}{2}$	$1s2s^2 2p^6$	^2S	$\frac{1}{2}$	4.708 29	0.427	8.326 69	0.391
$1s^2 2s^2 2p^5$	$^2P^\circ$	$\frac{3}{2}$	$1s2s^2 2p^6$	^2S	$\frac{1}{2}$	4.711 07	0.216	8.328 51	0.197

density of charge of electrons depend on adjustable parameters which are determined by minimizing the total energy of one level or of several weighted levels. The Lamb shift correction is evaluated from hydrogenic formulas, the nuclear charge Z being replaced by an effective charge Z^* derived from one-electron energies. Calculation of the energies for all the levels of the complex of the lowest configurations $1s^2(2s+2p)^N$ and of the core-excited complex $1s(2s+2p)^{N+1}$ has been performed at the first order of perturbation theory by taking into account configuration mixing in both parities. In order to strengthen the consistency of the whole set, only the number N of external electrons has been varied in the calculation of the levels of the successive He-, Li-, Be-, B-, C-, N-, O-, and F-like ions.

For each ion, the following steps are (i) determination of the parameter set I which minimizes the total energy of the ground configuration (one parameter for the $n=1$ shell and another for the $n=2$ shell when Z is larger than 3); (ii) determination of the parameter set II which minimizes the average energy of the core-excited configurations; (iii) the ground-state energy being higher when calculated with parameter set II than with parameter set I, the difference between these energies is introduced as a correction for the diagonal matrix elements of all the configurations of the lowest complex; (iv) calculation of energies for the relativistic configurations and radial integrals for the Breit operator which is diagonalized.

Multiconfiguration wave functions have been used to derive radiative transition probabilities and oscillator strengths. It is stressed that experimental data were not considered throughout the whole process. More than 500 lines were calculated. In the model used to simulate the absorption spectra, we have retained all the transitions with an absorption oscillator strength $gf>0.01$, that is 271 lines for chlorine and 268 for aluminum. gf is the product of the ground-state degeneracy and the absorption oscillator strength. For the strongest transitions of chlorine and aluminum, Table II gives the levels involved in the transitions, the wavelengths, and the gf products. We have only included the transitions with $gf>0.5$ either for chlorine or for aluminum. We have also included the two F-like transitions which have small gf values. The complete table of transitions can be found in Ref. 25.

Using these data in the analysis of the experimental spectra and comparing them to the known position of the cold chlorine K edge, we have found a wavelength difference of only 4.2 ± 0.7 mÅ between theory and experiment. This difference is almost the same for all the ionic species. This systematic deviation is probably due to correlation effects which have been neglected in the same way for all the ions. These deviations are smaller than in earlier work in which the wavelengths were calculated by the Hartree plus statistical exchange relativistic (HXR) method.[6]

B. Ionic populations and absorption coefficient calculations

A detailed collisional-radiative model has been developed to predict the ground configuration population for the complex $1s^2(2s+2p)^N$ with N varying from 0 to 7 (He-like to F-like ions). For each ionic stage, three levels were taken into account: the ground level and the first two resonance levels. Level energies were calculated by using quasihydrogenic formulas with improved screening coefficients.[26] The levels were coupled via spontaneous decay, electron collisional excitation and deexcitation, collisional ionization, and radiative, dielectronic, and collisional recombination. Collision strengths were evaluated by the Van Regemorter formula.[27] For collisional ionization we have used the Lanshoff-Perez[28] formulation; collisional recombination was inferred by detailed balance. Radiative recombination was calculated from Seaton's results[29] and dielectronic recombination was evaluated following Burgess.[30] The rates of photoexcitation and photoionization induced by the Bi backlighter emission were found negligible in front of collisional rates at the high electron densities obtained in the chlorine layer. We have also checked that incorporating more excited levels does not change significantly the results.

The set of coupled equations relating the stationary values of the level populations was solved numerically using an implicit scheme. This was done for a given matter density and temperature. Absorption coefficients as a function of x-ray photon energy were obtained by using the RELAC results for the wavelengths, oscillator strengths, and statistical weights, and using a Doppler profile for each individual transition. Convolution with the measured instrumental profile allows us to generate synthetic spectra ready to be compared to the experimental data. In Fig. 3 we have plotted the absorption coefficient as a function of photon energy for four electron temperatures from 65 to 140 eV at a matter density of 0.2 g/cm^3. At low electron temperatures, the fluorine-like ion is dominant while at 140 eV the B- and Be-like ions give the much larger peaks in the absorption spectrum. These calculations show that only a limited number of ions are absorbing at a given density and temperature. This demonstrates that $K\alpha$ lines are good candidates for ionization and temperature measurements.

C. Hydrodynamic simulation of the experiments

The shape of the electron temperature gradient in the bulk of the target, the conversion efficiency of laser energy into x rays, and the absorption of backlighter x rays through the cold target have been modeled using an hydrodynamic code incorporating photon transport physics.

A one-dimensional, plane geometry, Lagrangian code (XRAD) using a fully implicit integration scheme for the solution of the conservation equations of mass density, matter velocity, and internal energy has been developed. Laser deposition by inverse bremsstrahlung and resonance absorption together with flux-limited electron conduction have been treated classically.[31,32] An accurate equation of state has been used[33] to close the system of conservation equations. This equation of state was found particularly useful to calculate the thermodynamic properties of the chlorinated plastic $(C_2H_2Cl_2)_n$. Photon

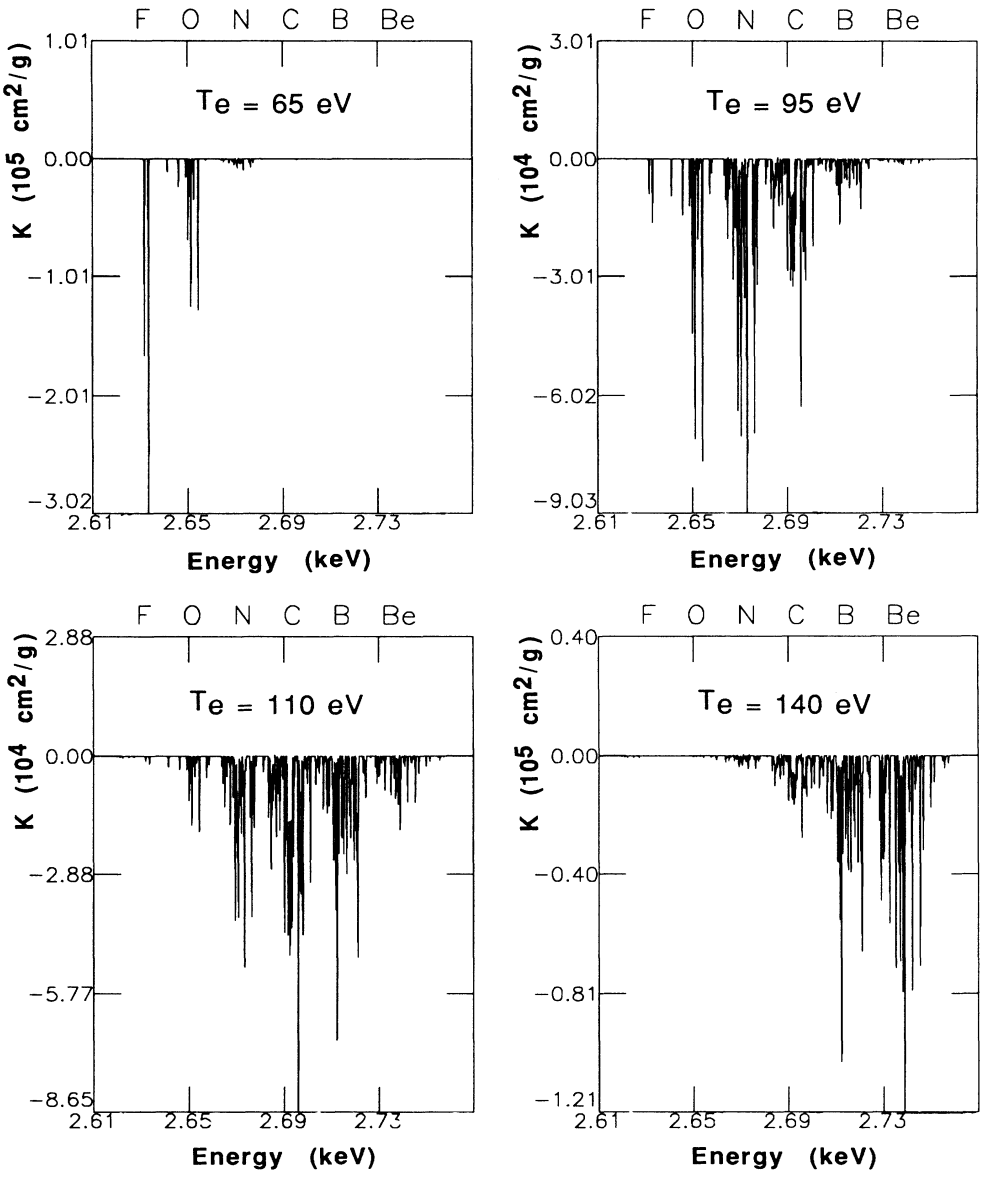

FIG. 3. Absorption spectrum of chlorine $K\alpha$ lines calculated in a one-temperature one-density model, for different electronic temperatures. Matter density is 0.2 g/cm^3. Absorption lines are Doppler broadened.

transport has been evaluated by using a multigroup, multiangle solution of the radiative transfer problem in the same way as in Ref. 32. The average charge state and the absorption and emission coefficients of chlorine and bismuth target layers have been calculated within the framework of the average-atom model under non-local-thermodynamic-equilibrium (LTE) conditions.[34,35] In this simple model, no attempts have been made to analyze the effects of photon reabsorption on the average charge state of the plasma. Front and rear side emission spectra, conversion efficiencies, and plasma parameter profiles can be calculated as a function of time and compared directly to experiment. No adjustable parameters have been incorporated in the code, apart from the flux limitation factor that we have set to its usual value of 0.03 at 0.26-μm laser wavelength.

IV. EXPERIMENTAL RESULTS

A. Measurements of $K\alpha$ absorption

Figure 4 shows typical time-integrated spectra obtained with the crystal spectrographs. They have been obtained with a target consisting of 0.4-μm-thick layer of bismuth on top of 12.5 μm of chlorinated plastic, illuminated with 4×10^{14} W/cm^2 incident laser intensity. Figure 4(a) shows the emission spectrum measured at the

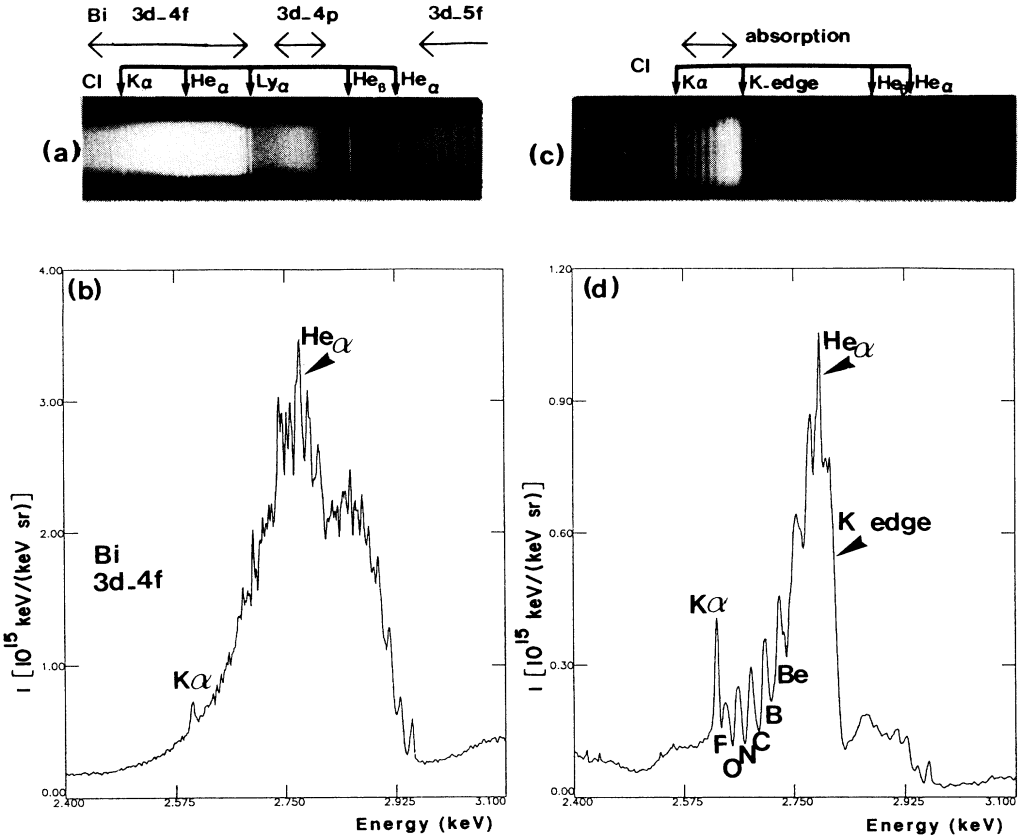

FIG. 4. Time-integrated spectra obtained with 4×10^{14}-W/cm^2 laser intensity incident onto a Bi-Cl target (0.3 μm of Bi). Film data (a) and densitometer tracing (b) of the front emission spectrum; film data (c) and densitometer tracing (d) of the rear absorption spectrum.

front of the target. Bismuth $3d$-$4f$, $3d$-$4p$, and $3d$-$5f$ unresolved transition arrays appear as weak lines superimposed on broadbands of quasicontinuum radiation. Chlorine lines are also present on this spectrum: the $K\alpha$ line emitted by the cold target, the heliumlike $1s^2$-$1s2p$ (called hereafter He_α) including the resonance, intercombination, and dielectronic satellite lines, and at shorter wavelength, other lines of the He-like and H-like Rydberg series. In Fig. 4(b), we have shown the densitometer tracing obtained from this picture in the region of the chlorine $K\alpha$ absorption lines. It shows that between the cold $K\alpha$ and the He_α lines, the bismuth emission is a smooth continuum with slowly varying intensity.

Figure 4(c) shows the time-integrated absorption spectrum obtained at the rear of the target and Fig. 4(d) is the corresponding densitometer tracing. In Fig. 4(c), $K\alpha$ chlorine absorption lines appear as broad dark features, one for each ion species. They are due to the superimposition of many broadened transitions corresponding to a single ion, as shown in Sec. III B. In Fig. 4(d) they are labeled by the isoelectronic series of the corresponding absorbing chlorine ion. It should be noted that all the chlorine ions, from neutral to hydrogenlike are present either in emission or in absorption. In Bi-Cl experiments, He- and Li-like ions are always emitting. The appearance of the He_α line in emission whatever the thickness of the bismuth layer (up to 2 μm) seems to be due to large spatial variations of the ablation depth across the focal spot diameter. This could be attributed to hot spots in the laser focus intensity distribution or to inhomogeneities in the bismuth thickness. The unshifted K edge and the emitting $K\alpha$ line of cold chlorine corresponding to ions less ionized than the F-like ion (Cl^{8+}) can also be seen clearly.

Figure 5 shows a time-resolved spectrum in the 2.6–2.9-keV region obtained with 2×10^{15} W/cm^2-laser intensity incident onto a Bi-Cl target with a 0.3-μm-thick Bi layer. It shows raw data obtained on the streak camera film as well as a three-dimensional (3D) plot of the microdensitometer tracing showing intensity on film as a function of time and energy. The emission lines appearing at both ends of the spectrum are the cold chlorine $K\alpha$ line and the He_α line. The bismuth continuum is emitted mainly near the peak of the laser pulse, when the laser intensity is high enough to reach electron temperatures where intense $3d$-$4f$ band emission occurs in the bismuth layer. Time evolution of the backlighter emission at the front and at the rear of the target has been calculated with the code XRAD. We found, in agreement with streak measurements, that bismuth emission follows closely the laser pulse with a delay of less than 200 ps.

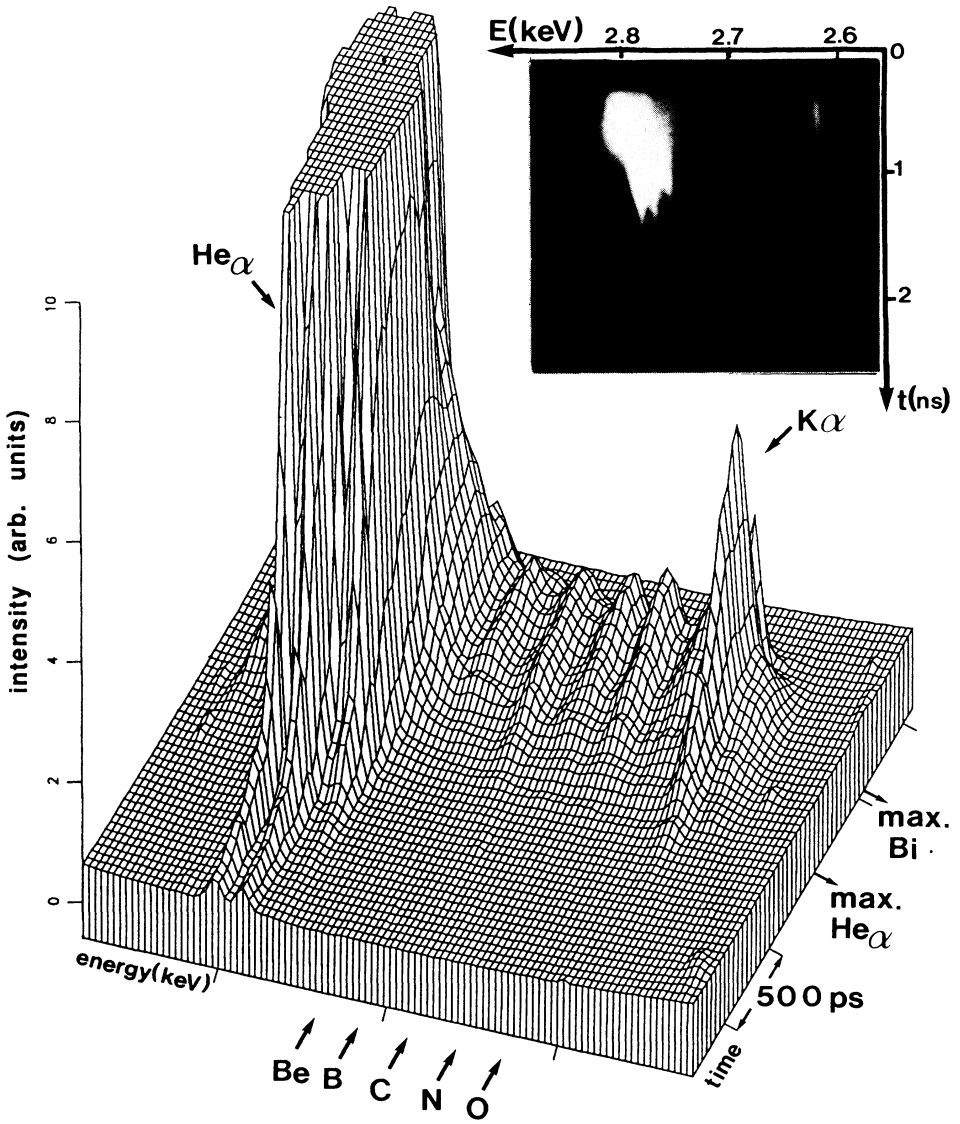

FIG. 5. Time-resolved spectra obtained with 2×10^{15} W/cm^2 laser intensity incident onto a Bi-Cl target (0.3 μm of Bi). 3D plot of the intensity function of time and photon energy. The maximum of He_α line emission has been cut to show more clearly the absorption lines. In the upper right corner, raw film data obtained with the streak camera.

Absorption lines are clearly seen on the bismuth continuum and the chlorine line emission lasts much longer than the laser pulse. The maximum of emission of the chlorine He_α line occurs at a later time than the maximum of bismuth emission. This time difference (550 ps) can be attributed to the ablation time of the bismuth layer.

Figure 5 shows that the absorption features corresponding to all the ions from F-like to Be-like are present during the whole time bismuth is emitting and that their time variation is weak. The appearance of all the absorption lines at the same time is a direct evidence of a temperature gradient in the chlorinated plastic along the line of sight of the spectrograph. Indeed, calculations performed at a given temperature show that the ionic distribution is peaked around a single ion, as previously noted in Sec. III B.

B. Temperature gradients

These data can be unfolded to give the line of sight integrated optical depth and the temperature gradient in the absorbing plasma. We have used only the time-integrated data since time-resolved absorption line intensities were too weak for a quantitative analysis. To get the optical depths corresponding to each ion species we have followed the procedure described below.

The spectral shape of the backlighter intensity is a key parameter in determining the zero absorption level in the rear spectra. We have checked that the spectral shape of

the bismuth continuum emerging from the rear of the target was the same as the emission at the front by performing an experiment where the chlorinated plastic was replaced by Mylar. Accordingly, the zero absorption level was determined by adjusting the shape of the front bismuth spectrum to the edges of the absorption spectral interval at 2575 and 2750 eV.

The absorption coefficient $K(\nu)$ is then calculated using the usual absorption formula:

$$I(\nu)=I_0(\nu)e^{-K(\nu)\Delta r}, \tag{1}$$

where ν is the frequency of the x-ray photon, I and I_0 the absorbed and incident x-ray intensities, and Δr the absorbing region thickness along the line of sight, i.e., along the normal to the target.

A value of the space-integrated average density $(\rho\Delta r)_i$ in the absorbing region for each given ionic species i has been calculated from the time-integrated experimental spectra, assuming that the lines corresponding to a given ion can be approximated as a single line.[25] For low absorption (i.e., $I_0/I<10$), the $(\rho\Delta r)_i$ for a given ion can be written

$$(\rho\Delta r)_i=\frac{M_i}{\sigma_0}\int_{\Delta\nu}\ln\left[\frac{I_0}{I(\nu)}\right]d\nu, \tag{2}$$

where $\sigma_0=\pi e^2\langle f_i\rangle/mc$; e and m are the charge and the mass of the electron, M_i the mass of the atom, c the speed of light, and $\langle f_i\rangle$ is the oscillator strength averaged over the lower states and summed over the upper states of the

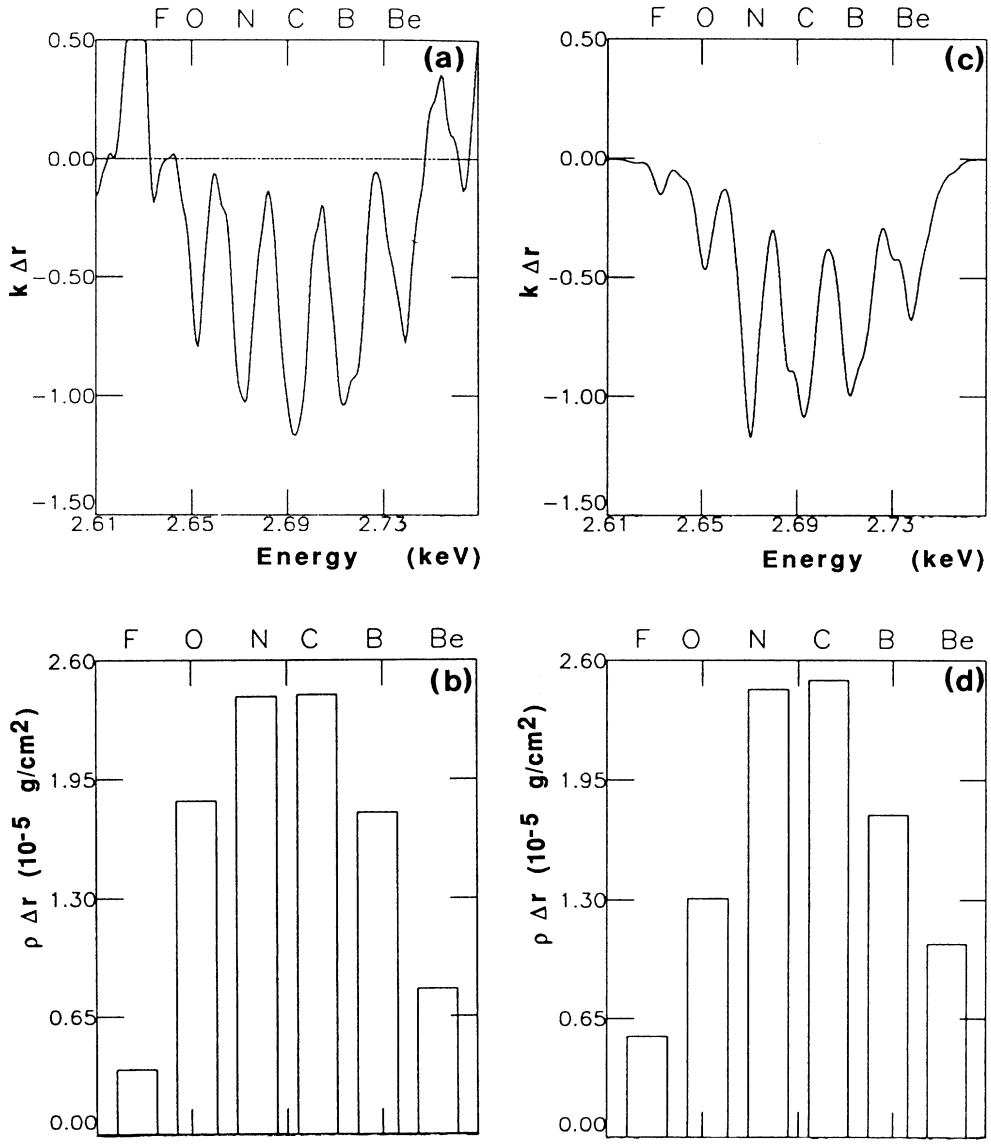

FIG. 6. Comparison of experimental [(a) and (b)] and calculated [(c) and (d)] optical depths and apparent $(\rho\Delta r)_i$ for a shot at 7.4×10^{14} W/cm^2 laser intensity.

$K\alpha$ lines of the ion labeled i. In Eq. (2), the range $\Delta\nu$ of the integral is the spectral interval in which the ion labeled i is absorbing. Previous works assumed that this low absorption assumption was valid.[6,8] In fact, among the many lines involved for a given ion, some of them have a so large oscillator strength that they absorb completely the backlighter emission. Then, the expression (2) is no longer equal to the average density for a given ion i, but it still remains dependent on electron temperature.[25] In the following, we have used these apparent $(\rho\Delta r)_i$ to adjust the experimental absorption to theory. Figure 6 shows an example of the analysis of the absorption results obtained for a laser shot at 7.4×10^{14} W/cm^2 laser intensity incident on a Bi-Cl target with a 0.3-μm-thick bismuth layer. Figure 6(a) shows an example of the measured optical depth as a function of photon energy and Fig. 6(b) gives the apparent $(\rho\Delta r)_i$ calculated for each ion species.

In all the measured absorption spectra, too many ionic structures appear at the same time to be excited at only one given temperature, as shown in typical shots in Figs. 4–6 (4.0×10^{14}, 2.0×10^{15} W/cm^2, and 7.4×10^{14} W/cm^2 laser intensity onto a 0.3-μm Bi layer). As already noted before, this is an indication of the presence of a temperature gradient in the heated chlorinated plastic. The peak of the ion distribution gives an estimate of the average temperature. Comparison of experimental optical depths and apparent $(\rho\Delta r)_i$ with simulations taking into account a spatial variation of the temperature inside the heated target allows a measurement of the electron-temperature gradient.

Accordingly, we have extended our one-density, one-temperature model to allow for the calculation of the optical depth in a nonhomogeneous temperature plasma. This was done by modeling, in plane geometry, the shape of an arbitrary gradient with a limited number of temperature zones with variable widths. A fit to the measured apparent $(\rho\Delta r)_i$ was obtained by adjusting these widths and the value of the electronic temperature in each zone. For most of the shots, nine different temperatures in the range 50–150 eV were found sufficient to provide an agreement within 10% between the measured and calculated apparent $(\rho\Delta r)_i$. Matter density was kept constant in this simulation. This was supported by hydrocode simulations which show only little density changes over the depth range where significant absorption occurs. Moreover, the model described in Sec. III B have shown that the absorption coefficients were not very sensitive to matter density.[25] We have introduced only F-like to Be-like ions since Li- and He-like absorption lines were obscured by the emission from the front of the chlorinated plastic foil.

Figures 6(c) and 6(d) show the result of the fitting procedure for the optical depths and the $\rho\Delta r$, respectively. Matter density was kept constant to 0.2 g/cm^3 in the calculations. The absorption spectrum of Fig. 6(a) is well reproduced by the simulation [see Fig. 6(c)]. The apparent $(\rho\Delta r)_i$ obtained for O-like to B-like ions are in good agreement with experiment. The discrepancy for the F-like ion can be easily explained by noting that the corresponding absorption line is blended with the cold $K\alpha$ emission line as shown in Fig. 4(d).

In this particular shot, we note that N- and C-like ions are the dominant species. The average electronic temperature obtained for the best fit is about 100 eV. For a lower laser intensity of 3.8×10^{14} W/cm^2, we have obtained a slightly lower temperature of about 70 eV. In that case, the dominant ion species were O- and N-like ions. The corresponding temperature gradients obtained for these two shots are shown in Fig. 7 (squares and triangles). At higher intensity, temperature is decreasing slowly towards the inside of the cold chlorine layer and this gradient shape is characteristic of the high-energy laser shots we have performed. At lower intensity, the temperature gradient is much steeper.

Figure 7 also shows the temperature gradient shapes obtained from the code XRAD for laser intensities of 6×10^{14} W/cm^2 and 3×10^{14} W/cm^2. To take into account time-integration effects, we have weighted the temperature values by the calculated time-dependent emissivity of the bismuth backlighter. The overall agreement between the experiment and the code is remarkable for the shape of the gradient as well as for its evolution as a function of laser intensity. Looking in more detail, we find a disagreement of about 20 eV on the absolute value of the average electron temperature for the higher intensity. For the lower intensity, code results show that the gradient is steeper and that the difference between calculations and experimental points is much larger. Several effects can account for this discrepancy. First, the code XRAD is a one-dimensional (1D) code and two-dimensional (2D) effects are likely to occur under the rather tight focusing conditions that we have used in the experiments. Secondly, after frequency-quadrupling, large laser intensity variations over the focal diameter can be found in typical shots. Thus, the calculated gra-

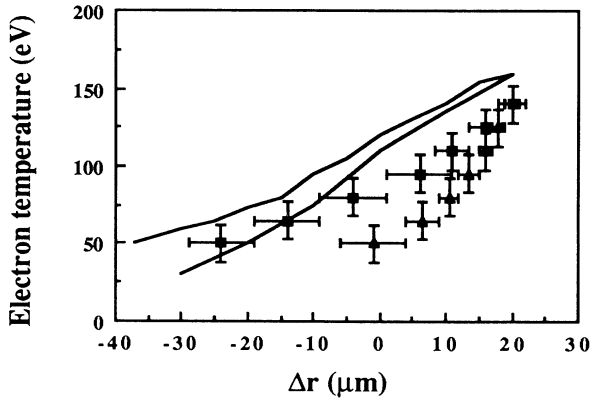

FIG. 7. Comparison of the measured and calculated temperature gradients in the dense chlorinated plastic foil. Hydrocode calculations (solid lines) are performed at laser intensities of 6×10^{14} W/cm^2 (upper curve) and 3×10^{14} W/cm^2 (lower curve). Experimental profiles are obtained for 7.4×10^{14} W/cm^2 (squares) and 3.8×10^{14} W/cm^2 (triangles). Horizontal error bars correspond to the width of the temperature zones used in the analysis of the experiment.

dient shape must be weighted by a complex distribution of laser intensities to give a meaningful comparison with experiment. Moreover, the surface condition of the bismuth layer was not measured in these experiments and could also be a possible reason for a nonhomogeneous heating of the foil.

C. X-ray heating of the target

The slow temperature decrease observed (see Fig. 7) as a function of position in the dense part of the target around 100 eV is difficult to explain by thermal heating. Simulations using the one-dimensional hydrocode FILM,[36] which do not include radiative transport, indicate a steep temperature gradient in the thermal front with a temperature of only a few eV in the dense target. Smooth temperature gradient shapes, as observed here, can be explained by radiative preheating of the target and has been seen previously for high-Z plasmas in simulations where this effect was included.[34,37]

The dynamics of radiative preheating of a cold target by soft x rays has been reviewed comprehensively in Ref. 37. Qualitatively, the plasma region with electron temperatures of the order of 1 keV and densities lower than 0.1 g/cm^3 acts as a conversion layer of thermal energy to soft x rays. This region is optically thin to its own radiation. The x rays generated in the conversion layer deposit their energy deeper in the cold target where they generate a radiation heat wave with electronic temperatures of order 100 eV and densities around 0.1–1 g/cm^3. This region is optically thick and reemission of blackbody radiation through the conversion layer contributes to the overall conversion efficiency.

To study in more detail the radiative energy balance, we have performed low spectral resolution x-ray measurements of the emission and absorption of the high-Z material x rays in the target. Figure 8 shows the emission spectra measured at the front of the target with the diode spectrometer and with the grating spectrograph. This shot has been obtained with 4.2×10^{14} W/cm^2 incident laser intensity onto a Bi-Cl target with a 0.75-μm-thick bismuth layer. The absolute intensity has been obtained from the diode signals. On these spectra, we can see that most of the xuv energy is emitted in the 0.5–1.5-keV range. A good agreement is found between the two sets of data in their common spectral range (0.1–1.5 keV). In the sub-keV (0–1 keV) and in the keV (1–4 keV) range, the spectrum of bismuth ($Z=83$) is very similar to the well-known spectrum of gold ($Z=79$).[12,19,38] The spike on the grating spectrum at very low energies is probably due to the background noise associated to the rather high fog level of the film (low-energy photons are more widely spread on the film).

We measured the front xuv spectra for different thicknesses of the bismuth layer (0.3, 0.75, and 1.5 μm) results show essentially no differences in the absolute intensity and shape of the emissions. This proves that reemission processes from the radiation heat wave are negligible and that the conversion layer optical depth is constant when the thickness of bismuth changes. Therefore, we assumed that the rear xuv spectrum was very close to the measured one emitted towards the front of the target.

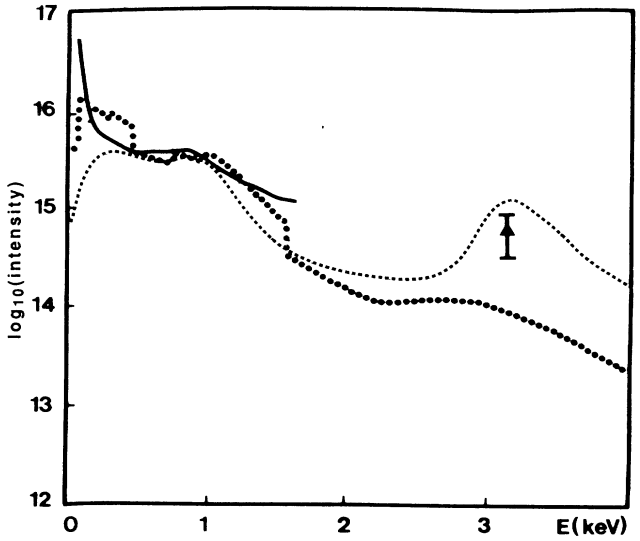

FIG. 8. Low resolution x-ray spectra in the range 0–4 keV. X-ray intensities are in keV/keV/sr. Diodes (dots) and grating (solid line) spectra are obtained with 4.2×10^{14} W/cm^2 laser intensity onto a 0.75-μm-Bi layer. The theoretical spectrum (dashed lines) has been obtained with the code XRAD at 5×10^{14} W/cm^2. The $3d$-$4f$ UTA intensity measured by crystal spectroscopy is also reported (triangle).

In Fig. 8 we have plotted the spectrum calculated by XRAD for a laser intensity of 5×10^{14} W/cm^2 at 0.26 μm, taking into account the measured size of the focal spot (assumed constant over the whole spectral range). We recognize the broadband O and N spectra at 200 and 1000 eV, respectively and the M-band spectrum around 3.2 keV corresponding to the $n=4$ to $n=3$ transition arrays used as a backlighter. On an absolute basis, the spectra measured with the diode spectrometer compares very well with code predictions in the 0.1–2.5-keV range. Using the calculated reflectivity of the PET crystal, film calibration, filter attenuations, and the measured geometrical parameters of the spectrograph, it was possible to get the absolute intensity emitted over the whole band of the $3d$-$4f$ transition array with about a factor of 2 accuracy. As shown in Fig. 8, good qualitative agreement is found between code calculations and this measurement. The intensity measured with the diode spectrometer above 3 keV is about 1 order of magnitude smaller than code predictions. It is known[12] that the accuracy in diode measurements is greatly improved if many channels overlap. This was not the case for the two p-i-n diode channels which had a small overlap with the XRD channels above 3.5 keV. The same discrepancy was found between XRAD and diode spectrometer results in copper.[39]

Figure 9 shows the grating spectrograph results measured during the same shot at the front and at the rear of the target (laser intensity of 4.2×10^{14} W/cm^2 onto a Bi-Cl target with 0.75-μm-thick Bi layer). Absorption of x rays in the target in the 0.3–1.5-keV range can be clearly seen from the data. The absorbed spectrum is a factor 50

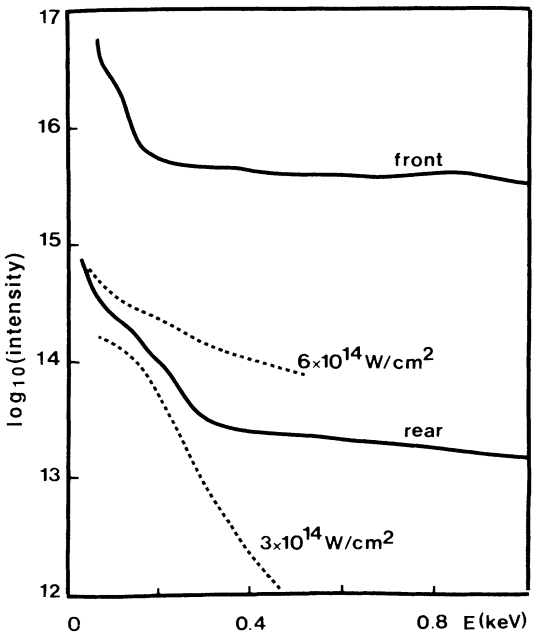

FIG. 9. Comparison of the spectra measured at the front and the rear of the target with the grating spectrograph. X-ray intensities are in keV/keV/sr. Shot conditions: 4.2×10^{14} W/cm^2 onto a Bi-Cl target with a 0.3-μm-thick Bi layer. XRAD code predictions of the rear spectrum (dashed lines) are reported for laser intensities of 3 and 6×10^{14} W/cm^2.

to 80 lower in intensity. The xuv emission has almost been suppressed at the rear of the target. This effect can be quantified by integrating the sub-keV signals from 100 to 750 eV: at the front, 16% of the laser energy is converted to sub-keV x rays and only 0.25% of the laser energy is found in the rear sub-keV x ray emission. In Fig. 9 we have also compared the rear grating spectrograph results to code predictions at 3×10^{14} W/cm^2 and 6×10^{14} W/cm^2 in the 0–500-eV range. Again, the agreement is qualitatively good between the two sets of results. This means that absorption coefficient calculations are quite reliable in the chlorinated plastic layer despite the fact that we have simulated the absorption and emission properties of $(C_2H_2Cl_2)_n$ by assuming that the layer was pure chlorine with a dilution factor corresponding to the mass percentage of chlorine into the chlorinated plastic.

D. Samarium-aluminum experiment

The results of the Bi-Cl experiment have been supplemented in a second series of measurements in which the absorber was a thin aluminum layer. The purpose of this study was to vary the distance between the heating material and the absorber to get more details on the shape of the electron-temperature gradient. The aluminum layer had to be very thin to ensure a uniform temperature distribution in the absorbing region. A thickness of 7000 Å was found sufficient to meet this criterion and to get measurable absorption. Aluminum was chosen because it can be deposited easily on a plastic substrate. Samarium was used as a backlighter material since its $3d$-$4f$ UTAs fall in the same spectral range than the aluminum $K\alpha$. However, the samarium spectrum[15,16,25] in the 1.3–1.6-keV range was found more spiky than the bismuth spectrum and it was more difficult to take into account the backlighter intensity in the absorption spectra, as described in Sec. IV B.

Figure 10 shows the results obtained for a laser intensity of 3×10^{14} W/cm^2 when the aluminum layer position was varied inside the target. Figure 10(a) was obtained with aluminum just behind samarium. In Figs. 10(b)–10(d) a Mylar spacer of thickness 1.5, 3.5, and 6 μm, respectively, was inserted between the emitter and the absorber. The temperature variation in the aluminum layer as a function of Mylar thickness is clearly demonstrated in this figure. In case (a), He-like to C-like absorption lines can be seen with dominant Li- and Be-like ions. In case (d) (6 μm of Mylar), aluminum is much colder and absorbs mostly on F- and O-like lines. It can be noted that in this aluminum experiment $K\alpha$ lines are not emitting, and that He- and Li-like lines are observed in absorption unlike the chlorine case. This could be due to the better quality of the backlighter layer or of the laser focal spot. In addition, samarium has a lower heating capability than bismuth: it has a much lower Z and its xuv emission is a factor of 10 lower, centered at lower energies (around 300 eV).[25,40] For each Mylar layer thickness, we have estimated from other shots the emission spectrum in the absorbing spectral region (see the dashed lines in Fig. 10). We have then been able to calculate the absorption coefficients corresponding to each aluminum ionic species with the model described in Sec. III B.

Analyzing the experimental spectra of Fig. 10, we have then obtained the shape of the electron-temperature gradient as a function of the aluminum tracer depth inside Mylar, as shown in Fig. 11 (dots). The probed temperature is smaller in the case of aluminum compared to chlorine since the Z of the heating material is lower. Due to the smaller thickness of the absorber, the ionic distribution is much more peaked in aluminum than in chlorine indicating that the temperature was nearly uniform in the absorbing region. Despite the fact that the absorbing thickness is much smaller in aluminum, the optical depth is larger or, at least, comparable to the chlorine case. This is due to to larger absorption coefficients and to higher matter density of aluminum, compared to chlorine. Aluminum $K\alpha$ lines appearing at lower temperatures, this particular experiment probes a temperature region where the gradient length is much larger than in chlorine.

Results from the code XRAD are also shown in Fig. 11, indicating a very good agreement with experiments. However, as noted in the chlorine experiments, the temperature of the preheated region at the absorber-emitter interface is always much larger in the code than in the measurements. This can be due to a systematic overestimate of the absorption coefficient of the plastic layer in the spectral range (below 1 keV) where most of the radiative to thermal energy conversion occurs.

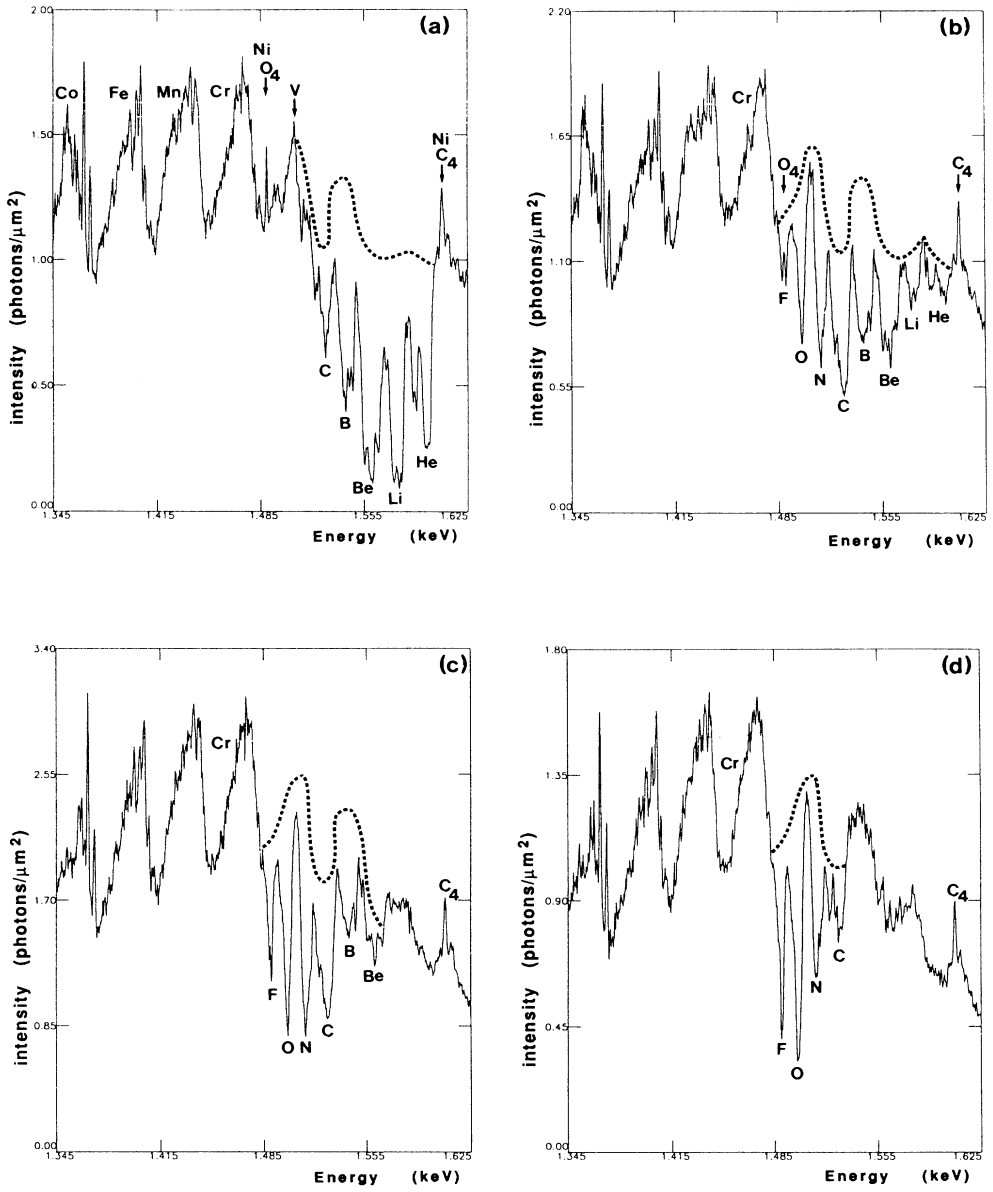

FIG. 10. Aluminum absorption spectra obtained with Sm-Al targets for different thicknesses of the Mylar spacer between Sm and Al. (a) 0 μm; (b) 1.5 μm; (c) 3.5 μm; (d) 6 μm. The estimated front intensity is traced (dashed lines).

V. CONCLUSION

This work has shown that $K\alpha$ absorption spectroscopy is a very powerful diagnostic in plasma regions which cannot be probed by emission spectroscopy. It can lead to a measurement of the ionic state, the electronic temperature gradient, and integrated density in the absorbing region. For the first time, we have experimentally determined the shape of the shallow temperature gradient behind the conduction zone. These experiments have been complemented by xuv spectra measurement and hydrocode simulations.

Atomic structure calculations play an important role in the absorption diagnostic at different stages of the analysis of experimental results. Indeed, the wavelengths and oscillator strengths have to be calculated for the absorbing material. Here, we have performed such calculations for chlorine and aluminum. The comparison of the experimental and calculated wavelengths with the code RELAC enabled improvements in the calculations from previous works. Good agreement has been found between calculated and measured spectra, including the shape of each ion absorption structure which is very sensitive to the calculated oscillator strengths.

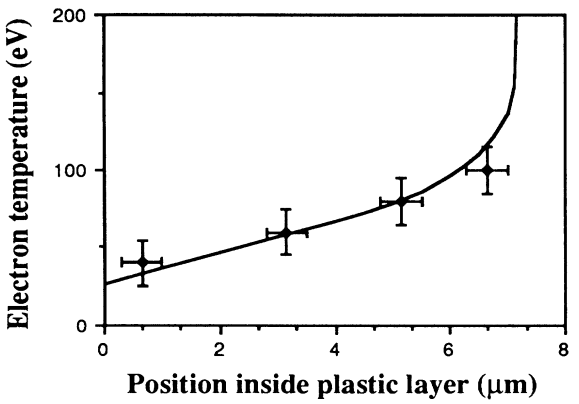

FIG. 11. Electron temperature as a function of the position of the aluminum layer behind samarium for a laser intensity of 3×10^{14} W/cm^2. Horizontal error bars represent the aluminum layer thickness (0.7 μm). The solid line gives the XRAD results with the same laser intensity.

The results presented in this paper clearly demonstrate that the high-Z layer heated by the laser beam emits x rays in the range 0.5–1.5 keV which are absorbed in the dense low-Z absorber plasma. These photons heat the absorbing layer at temperatures around 100 eV, with a shallow temperature gradient. This had been predicted in earlier simulations of radiative transport in high-Z plasmas. The comparison of our experimental data with the radiative hydrodynamic code XRAD has shown that this radiative heating occurs also in dense low-Z plasmas. The good agreement between code and experimental data obtained with the different diagnostics set up in the experiment give some confidence in the rather crude nonlocal thermodynamic equilibrium calculations of bismuth emissivities in the sub-keV and in the 3–4-keV range. We are now performing further experiments and calculations to study the time evolution of the plasma parameters and of their dependence as a function of the heating element.

ACKNOWLEDGMENTS

We would like to acknowledge the help given during the experiments by the laser technical team of the LULI. Densitometry of the films was made at the Centre de Densitomètrie et de Synthése d'Images (CDSI) at Orsay University. Fruitful discussions with M. Klapisch were very helpful during the early stage of that work.

[1]A. Hauer, *Spectral Line Shapes* (Walter de Gruyter & Co., New York, 1981), p. 295, and references therein.
[2]J. D. Kilkenny, R. W. Lee, M. H. Key, and J. G. Lunney, Phys. Rev. A **22**, 2746 (1980).
[3]P. G. Burkhalter, M. J. Herbst, D. Duston, J. Gardner, M. Emery, R. R. Whitlock, J. Grun, J. P. Apruzese, and J. Davis, Phys. Fluids, **26**, 3650 (1983).
[4]P. Alaterre, C. Chenais-Popovics, P. Audebert, J. P. Geindre, and J. C. Gauthier, Phys. Rev. A **32**, 324 (1985).
[5]N. H. Burnett, G. D. Enright, A. Avery, A. Loen, and J. C. Kieffer, Phys. Rev. A **29**,2294 (1984).
[6]A. Hauer, R. W. Cowan, B. Yaakobi, O. Barnouin, and R. Epstein, Phys. Rev. A **34**, 411 (1986).
[7]D. K. Bradley, J. D. Hares, and J. D. Kilkenny, Rutherford Appleton Laboratory, Annual Report No. RL-83-043, p. 5.4, 1983 (unpublished).
[8]C. Chenais-Popovics, C. Fievet, J. P. Geindre, J. C. Gauthier, J. F. Wyart, E. Luc-Koenig, SPIE Proceedings **831**, 30 (1987).
[9]P. Audebert, D. K. Bradley, M. C. Richardson, R. Epstein, P. A. Jaanimagi, O. Barnouin, J. Delettrez, B. Yaakobi, F. J. Marshall and B. L. Henke, SPIE Proceedings **831**, 9 (1987).
[10]E. Jannitti, P. Nicolosi, and G. Tondello, Physica **124C**, 139 (1984); E. Jannitti, P. Nicolosi, and G. Tondello, J. Phys. (Paris) Colloq. **C1-49**, 71 (1988).
[11]H. Nishimura, F. Matsuka, M. Yagi, K. Yamada, S. Nakai, G. H. McCall, and C. Yamanaka, Phys. Fluids, **26**, 1688 (1983).
[12]P. Alaterre, H. Pèpin, R. Fabbro, and B. Faral, Phys. Rev. A **34**, 4184 (1986).
[13]J. Bauche, C. Bauche-Arnoult, and M. Klapisch, Adv. At. Mol. Phys. **23**, 131 (1988).
[14]N. Tragin, J. P. Geindre, P. Monier, J. C. Gauthier, C. Chenais-Popovics, J. F. Wyart, and C. Bauche-Arnoult, Phys. Scr. **37**, 72 (1988).
[15]P. G. Burkalter, D. J. Nagel, and R. R. Whitlock, Phys. Rev. A **9**, 2331 (1974).
[16]A. Zigler, M. Givon, E. Yarkoni, M. Kishinevsky, E. Goldberg, and B. Arad, Phys. Rev. A **35**, 280 (1987).
[17]C. Bauche-Arnoult, J. Bauche, E. Luc-Koenig, J. F. Wyart, R. M. More, C. Chenais-Popovics, J. C. Gauthier, J. P. Geindre, and N. Tragin, Phys. Rev. A **39**, 1053 (1989).
[18]B. L. Henke, J. Y. Uejio, G. F. Stone, C. H. Dittmore, F. G. Fujiwara, J. Opt. Soc. Am. B **3**, 1540 (1986).
[19]N. Tragin, Thèse de Doctorat, Paris XI University, Orsay, France, 1989.
[20]Y. M. Aleksandrov, M. O. Koshevoi, V. A. Murashova, T. F. Nikitina, A. A. Rupasov, G. V. Skilskov, A. S. Shikanov, M. N. Yakimenko, Y. A. Zakharenkov, K. Eidmann, R. Sigel, and G. D. Tsakiris, Laser Part. Beams **6**, 561 (1988).
[21]M. Chaker, H. Pepin, V. Bareau, B. Lafontaine, I. Toubhans, R. Fabbro, and B. Faral, J. Appl. Phys. **63**, 892 (1988).
[22]E. Luc-Koenig, Physica **62**, 393 (1972).
[23]M. Klapisch, J. L. Schwob, B. S. Fraenkel, and J. Oreg, J. Opt. Soc. Am. **67**, 148 (1977).
[24]E. Luc-Koenig, M. Klapisch, and A. Bar-Shalom, unpublished computer code RELAC.
[25]C. Fievet, Thèse de Doctorat, Paris XI University, Orsay, France, 1989.
[26]R. M. More, J. Quant. Spectrosc. Radiat. Transfer **27**, 345 (1982).
[27]H. Van Regemorter, Astrophys. J. **136**, 906 (1962).
[28]R. K. Landshoff and J. D. Perez, Phys. Rev. A **13**, 1619 (1976).
[29]M. J. Seaton, Mon. Not. R. Astron. Soc. **119**, 81 (1959).
[30]A. Burgess, Astrophys. J. **141**, 1588 (1965).

[31]C. E. Max, *Laser-Plasma Interaction,* edited by R. Baliant and J. C. Adam (North Holland, Amsterdam, 1982), p. 302.
[32]R. Ramis, R. Schmaltz, and J. Meyer-Ter-Vehn, Comput. Phys. Commun. **49**, 475 (1988).
[33]R. M. More, K. H. Warren, D. A. Young, and G. B. Zimmerman, Phys. Fluids **31**, 3059 (1988).
[34]J. C. Gauthier and J. P. Geindre, Laboratoire PMI, Ecole Polytechnique Report No. PMI 1971, 1988 (unpublished, available upon request from the authors).
[35]W. A. Lokke and W. H. Grasberger, Lawrence Livermore National Laboratory Report No. UCRL 52276, 1977 (unpublished).
[36]J. C. Gauthier, J. P. Geindre, N. Grandjouan, and J. Virmont, J. Phys. D **16**, 321 (1983).
[37]R. Sigel, J. Meyer-Ter-Vehn, G. D. Tsakiris, and S. Witkowsky, SPIE Proceedings, **831**, 73 (1987).
[38]M. Busquet, D. Pain, J. Bauche, and E. Luc-Koenig, Phys. Scr. **31**, 137 (1985).
[39]I. Toubhans, R. Fabbro, J. C. Gauthier, M. Chaker, and H. Pepin, Laboratoire PMI, Ecole Polytechnique, Report No. PMI 2143, 1989 (unpublished).
[40]C. Chenais-Popovics, C. Fievet, J. C. Gauthier, J. P. Geindre, J. F. Wyart, E. Luc-Koenig, SPIE Proceedings (to be published).

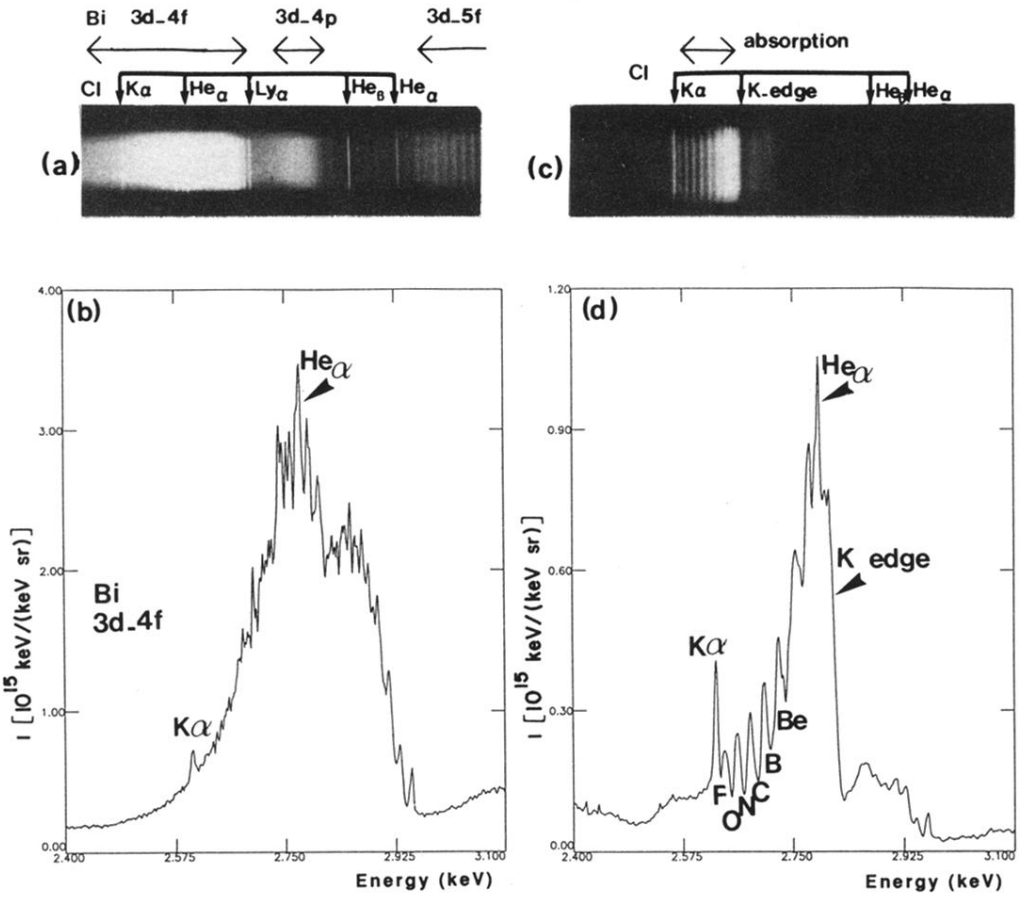

FIG. 4. Time-integrated spectra obtained with 4×10^{14}-W/cm^2 laser intensity incident onto a Bi-Cl target (0.3 μm of Bi). Film data (a) and densitometer tracing (b) of the front emission spectrum; film data (c) and densitometer tracing (d) of the rear absorption spectrum.

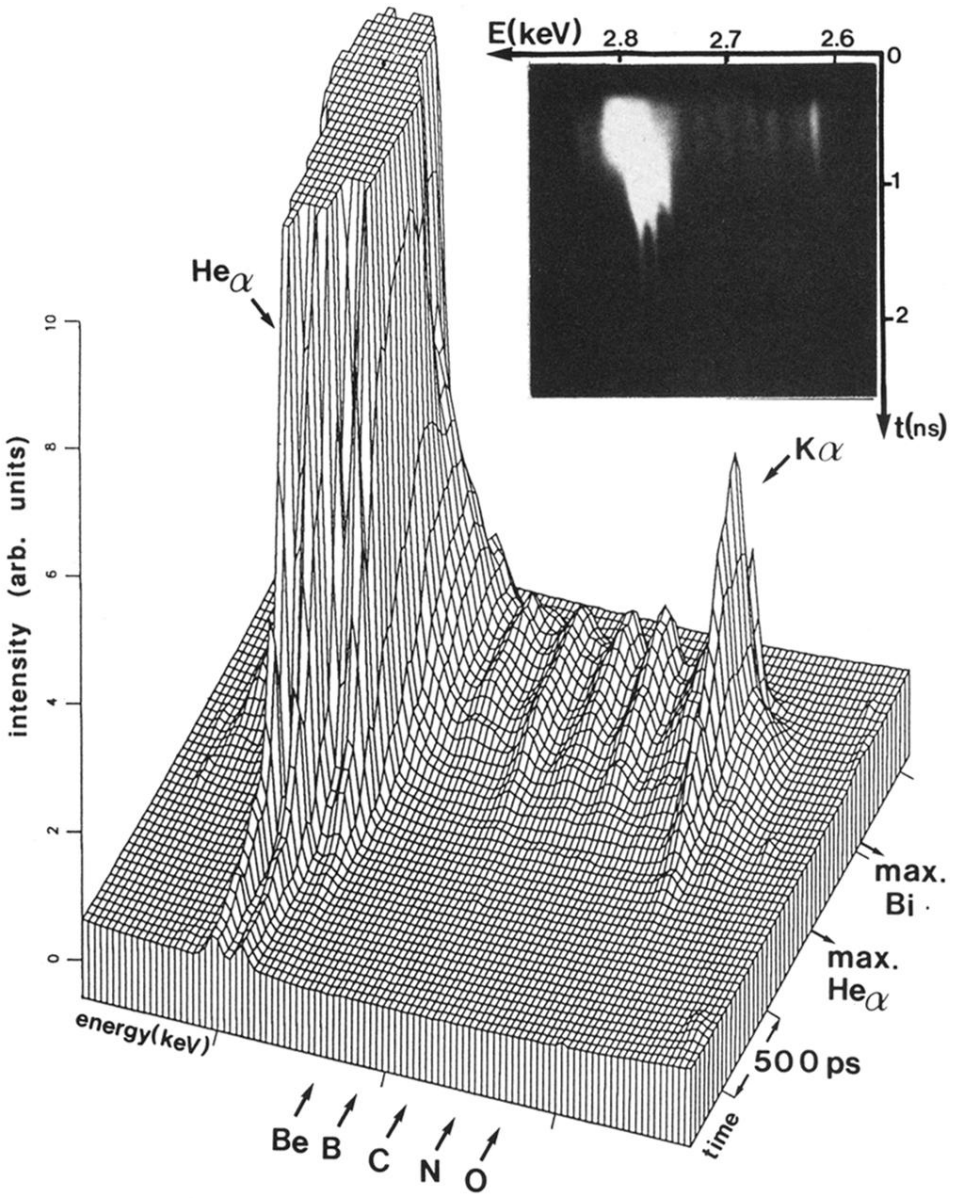

FIG. 5. Time-resolved spectra obtained with 2×10^{15} W/cm^2 laser intensity incident onto a Bi-Cl target (0.3 μm of Bi). 3D plot of the intensity function of time and photon energy. The maximum of He_α line emission has been cut to show more clearly the absorption lines. In the upper right corner, raw film data obtained with the streak camera.